CHEMISTRY OF MATERIALS
pubs.acs.org/cm Article

$FeSi_4P_4$ and $CoSi_3P_3$: Hidden Gems of Ternary Tetrel Pnictides with Outstanding Nonlinear Optical Properties

Ernesto Soto, Shannon J. Lee, Andrew P. Porter, Gayatri Viswanathan, Georgiy Akopov, Nethmi Hewage, Kui Wu, Victor Trinquet, Guillaume Brunin, Geoffroy Hautier, Gian-Marco Rignanese, Aaron J. Rossini, and Kirill Kovnir*

Cite This: Chem. Mater. 2024, 36, 8854−8863

ABSTRACT: Metal silicon phosphides have shown promise as nonlinear optical materials. To be practically useful and cheap, earth-abundant 3*d* transition metals are preferred over their scarcer and more expensive 4d and 5d counterparts. We developed a synthetic method to produce polycrystalline bulk powders and millimeter-sized single crystals of ternary compounds $FeSi_4P_4$ and $CoSi_3P_3$. Both studied compounds have noncentrosymmetric and chiral crystal structures with ordered Si/P arrangements as was confirmed by single-crystal X-ray diffraction and solid-state NMR. Despite the presence of the transition metal, $FeSi_4P_4$ and $CoSi_3P_3$ are semiconductors with direct band gaps of 1.3 and 1.6 eV, respectively, indicating low-spin d^6 electronic configuration for octahedral Fe^{2+} and Co^{3+}. Relative to reported sulfide materials, $FeSi_4P_4$ and $CoSi_3P_3$ small band gap semiconductors demonstrate an outstanding combination of second-harmonic generation (SHG) activity and laser damage threshold (LDT). Both studied materials are phase-matchable with a 2.09 μm laser and not only exhibit 2.5−3.0 times stronger SHG signal than that of the state-of-the-art $AgGaS_2$ standard but also demonstrate an LDT response of 2.3−2.5 times higher than that of $AgGaS_2$ (at 1.09 μm laser with a pulse width of 10 ns)—which is unprecedented for small band gap semiconductors.

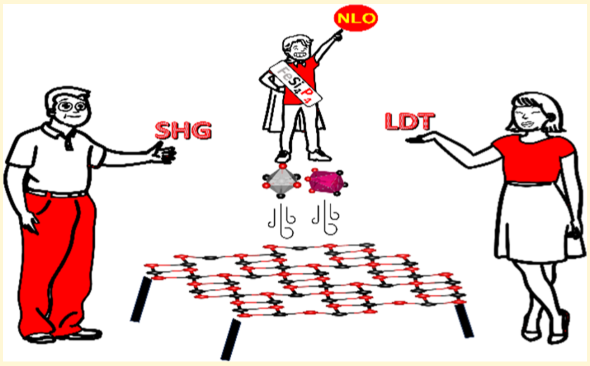

INTRODUCTION

The development of materials with improved performance, a sustainable nature, and cheap and abundant components is the mainstream direction of current materials research. Nonlinear optical (NLO) materials are crucial for the optics field due to their ability to upconvert frequencies of incoming light.[1−5] State-of-the-art NLO materials cover a significant part of the electromagnetic spectrum; however, there are still gaps, including the infrared (IR) region (2−20 μm). IR-NLO materials are important due to their application in optoelectronic devices, resource exploration, and long-distance laser communication.[1−5]

For second-harmonic generation activity, NLO materials must possess the following: (1) first and most crucial, noncentrosymmetric (NCS) crystal structure; (2) a semiconducting nature with suitable band gap for good transmission at the required spectrum region; (3) large second-harmonic generation (SHG) coefficients; (4) high laser damage threshold (LDT).[6−10] Currently, sulfides, such as $AgGaS_2$ and $LiInSe_2$, are used for IR-NLO applications.[11,12] In sulfides, a generally observed trend is that SHG is inversely proportional, and LDT is directly proportional to the band gap due to the polar nature of metal-chalcogen bonds, which prevents properties' optimization by simply adjusting the band gap.

A paradigm-shift approach to IR-NLO materials was recently offered by studies of metal tetrel pnictides (tetrel, *Tt*: Group 14 elements such as Si, Ge; pnictogen, *Pn*: group 15 elements such as P, As).[13−17] The presence of two nonmetal elements, like Si and P, with diverse bonding modes allows for the realization of noncentrosymmetric (NCS) structures for alkali-earth and rare-earth metal cations.[14−21] NCS structures are crucial for realizing properties such as piezoelectricity, pyroelectricity, chiral magnetism, and superconductivity.[22] When considering alkali, alkaline-earth, and rare-earth tetrel pnictides, the electropositive metal cation is surrounded by the most electronegative pnictogen atoms, and the nature of the metal−pnictogen interaction is essentially ionic. In ternary tetrel pnictides with a group of 8−11 transition metals, an assortment of crystal structures is formed with a mixture of

Received: June 17, 2024
Revised: August 22, 2024
Accepted: August 26, 2024
Published: September 3, 2024

https://doi.org/10.1021/acs.chemmater.4c01688

covalent metal−pnictogen and metal−tetrel interactions.[13,16,23,24] The only exception is chalcopyrite $MnSiP_2$ that does not have Mn−Si bonding.[13] In general, NCS metal tetrel pnictides exhibit a substantial combination of SHG and LDT.[25,26]

By analyzing several transition metal silicon phosphides (M−Si−P), we hypothesized that the more electropositive nature of Si leads to the π-electron back-donation between the filled *d*-orbitals of the transition metal and the empty antibonding Si−P orbitals, which is more effective than the π-electron back-donation between M and P.[24] These bonding preferences stabilize NCS local fragments such as linear Si−M−P, *cis*-MSi_2P_4, and *fac*-MSi_3P_3 units.[16,24,27] Similar trends were observed for heavier tetrel pnictides, with *cis*-MTt_2As_2 and *fac*-MSi_3As_3 building blocks.[17,23] The presence of direct covalent *Tt*−*Pn* bonding between these local units stabilizes the overall NCS crystal structure. When considering transition metal phosphides or silicides, the regular occurrence of an NCS structure is ∼15% statistically; however, a vast majority (95%) of ternary M−Si−P crystal structures are NCS for compositions with $M/(Si + P) < 1$.[28] For M−Si−P with *fac*-MSi_3P_3 building blocks, the strong ligand field nature of Si resulted in a low-spin electron configuration for transition metals. In turn, this leads to the formation of semiconducting phases for d^6 low-spin electronic configurations, such as Ru^{2+} or Ir^{3+}.[16] We have shown that $RuSi_4P_4$ and $IrSi_3P_3$ exhibit an outstanding combination of SHG and LDT despite both materials lacking phase-matching properties. Moreover, Ru and Ir are scarce and expensive metals. In this work, we developed cheaper and more earth-abundant alternative IR-NLO materials, $FeSi_4P_4$ and $CoSi_3P_3$. Both materials show phase-matchable properties with a 2.09 μm laser, better SHG performance for the largest studied particle size of ∼3.0 times for $CoSi_3P_3$ and ∼2.5 times for $FeSi_4P_4$, and >2 times increase in LDT with a 1.09 μm laser and a pulse width of 10 ns as compared to state-of-the-art $AgGaS_2$. In addition, the growth of millimeter-sized single crystals of the Fe- and Co-containing phases has been demonstrated herein. $FeSi_4P_4$ and $CoSi_3P_3$ are stable in acidic environments and when heated in air to at least 800 °C. The cost of the components is another advantage of the developed materials. The prices of the components to make 1 kg of NLO material based on the current element market price are $FeSi_4P_4$ (\$1.87), $CoSi_3P_3$ (\$9.86), $LiInSe_2$ (\$82.7), and $AgGaS_2$ (\$275.2).[29] Therefore, materials for $LiInSe_2$ and $AgGaS_2$ are approximately 50−150 times more expensive than those for $FeSi_4P_4$.

■ EXPERIMENTAL SECTION

$FeSi_4P_4$ and $CoSi_3P_3$ samples were synthesized in two steps: (1) arc-melting transition metal and silicon followed by (2) a reaction of metal silicide precursors with red phosphorus. Both materials were characterized by powder X-ray diffraction (PXRD), single-crystal X-ray diffraction (SCXRD), solid-state NMR (ssNMR), infrared (FTIR) spectroscopy, energy-dispersive X-ray spectroscopy (EDS), thermogravimetric analysis and differential scanning calorimetry (TGA/DSC), computations, diffuse reflectance spectroscopy, and NLO properties measurements (see Supporting Information for synthesis and methods details).

■ RESULTS AND DISCUSSION

The originally reported synthesis for $FeSi_4P_4$ and $CoSi_3P_3$ included a direct reaction from elements with subsequent grindings and long annealing periods to isolate bulk powder samples.[30,31] In addition, crystal growth using a Sn flux was reported. Cooling of the reaction mixture from 1127 to 777 °C at a rate of 1 °C/h (350h long) was reported to produce ∼0.2 mm diameter crystals.[30] A recent report by Yu et al. demonstrated the optimization of flux growth synthesis for $FeSi_4P_4$, which resulted in the isolation of ∼3 mm crystals using Sn flux and stoichiometric amounts of the respective elements.[32] However, there were no details of the synthetic optimization for the isolation of phase-pure bulk polycrystalline samples.

Our synthetic methods utilize arc-melted metal silicide precursors to obtain phase-pure samples.[16,20,33,34] This procedure guarantees the atomic mixing of the refractory constituents (M and Si), making the formation of binary M or Si phosphide admixtures less favorable. This is a new synthetic route for title materials, but similar approaches have been applied to prepare complex intermetallics.[35−39] $FeSi_4P_4$ and $CoSi_3P_3$ bulk powder samples were synthesized by stoichiometric reaction of a metal silicide precursor with elemental phosphorus, i.e., $FeSi_4 + 4\ P$ or $CoSi_3 + 3\ P$. The reactants were ground together and heated over 12 h to 1050 °C, annealed for 72 h, and then cooled to room temperature by turning off the furnace. This new synthetic route resulted in a significant reduction in reaction time from 2 weeks to 3.5 days and yielded a single-phase polycrystalline sample of $FeSi_4P_4$ (Figure S1) and a sample with the majority phase being $CoSi_3P_3$ (Figure S2).

Single crystals were grown using the arc-melted precursor, phosphorus powder, and Sn flux. The reaction products after molten Sn centrifugation were washed in a 1:1 HCl solution. On average, $2 \times 2 \times 1\ mm^3$ and $1 \times 1 \times 1\ mm^3$ sized crystals of $FeSi_4P_4$ and $CoSi_3P_3$ were isolated, respectively (Figures S1 and S2 insets). We found it necessary to go to higher temperatures and then slow cool to enhance crystal growth, which was previously utilized by Yu et al.[32] Since $CoSi_3P_3$ powder could not be produced in phase-pure form, property measurements were conducted by hand-selected single crystals, which were ground into powders for further characterizations.

$FeSi_4P_4$ and $CoSi_3P_3$ are acid and air stable after a couple of days and after 6 months of exposure to 1:1 $HCl{:}H_2O$ and air, respectively. Differential scanning calorimetry (DSC) measurements in evacuated and sealed silica ampules show that both stated compounds are thermally stable up to 1100 °C (Figures S3a,b and S4a,b). Both materials also have remarkable air stability at elevated temperatures. Thermal gravimetric analysis/differential scanning calorimetry (TGA/DSC) experiments in air reveal that $FeSi_4P_4$ is stable up to 900 °C. Thereafter, there is an inflection in the sample weight followed by an exponential increase up to 160 wt % (Figure S17a). The weight gain is complemented by the exothermic peak observed in the DSC (Figure S17a), which may indicate oxidation of the material, which was confirmed by PXRD analysis of the sample after the TGA experiment (Figure S17b). $CoSi_3P_3$ exhibits no substantial weight change to 800 °C and then a moderate increase in weight upon further heating but no visible peaks in the DSC (Figure S17a). PXRD shows that $CoSi_3P_3$ remains unchanged after heating in air to 1100 °C (Figure S17b). Therefore, we can state that both materials are stable against high-temperature air treatment and that $CoSi_3P_3$ is more stable than $FeSi_4P_4$.

$FeSi_4P_4$ was reported to crystallize in the noncentrosymmetric space group *P*1 (No. 1), with 1 Fe, 4 Si, and 4 P sites.[30] Our crystal structure solution agrees with the previously

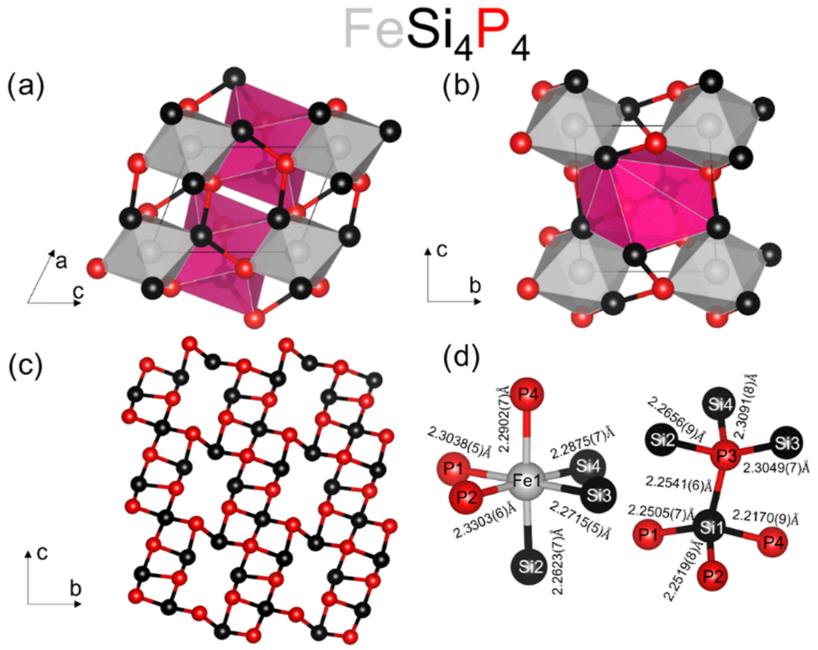

Figure 1. Crystal structure of $FeSi_4P_4$ (Fe: gray, Si: black, P: red). The unit cell is outlined in black. (a, b) General views showing *fac*-[$FeSi_3P_3$] octahedra (gray) and [$-P_3-Si-P-Si_3-$] trigonal antiprisms (dark pink). (c) Si−P network with Fe atoms omitted for clarity. (d) Isolated octahedral unit of *fac*-[$FeSi_3P_3$] and trigonal antiprism units of [$-P_3-Si-P-Si_3-$] with interatomic distances.

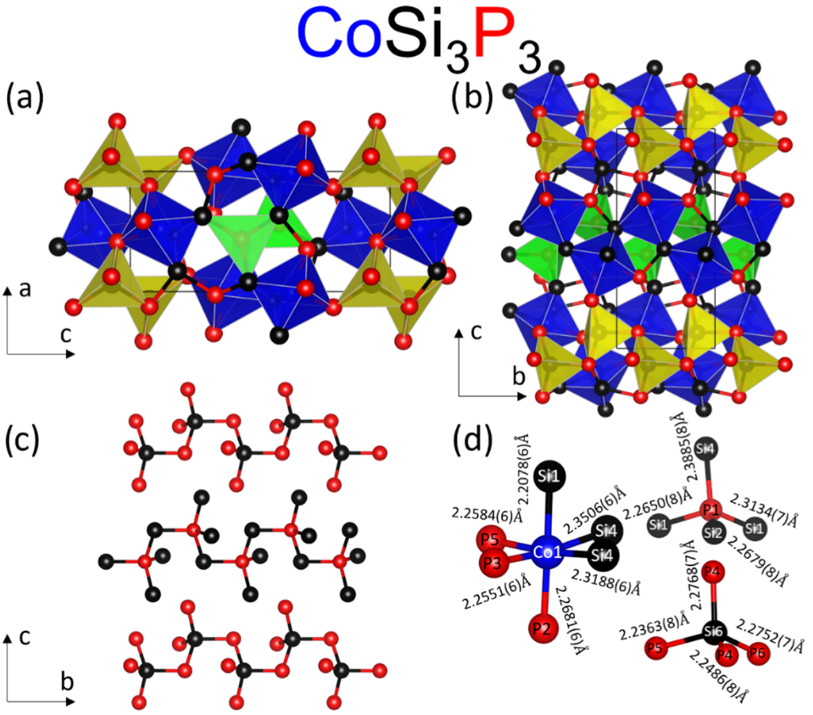

Figure 2. Crystal structure of $CoSi_3P_3$ (Co: blue; Si: black; P: red). The unit cell is outlined in black. (a, b) General views with *fac*-[$CoSi_3P_3$] octahedra shown in blue, [SiP_4] tetrahedra shown in yellow, and [PSi_4] tetrahedra in green. (c) Si−P network with Co atoms omitted for clarity. (d) Isolated octahedral *fac*-[$CoSi_3P_3$] and tetrahedral [SiP_4] and [PSi_4] units with interatomic distances.

reported structure with an R_1 value of 0.022 and a Flack parameter value of 0.012(7) (Table S1). In the crystal structure of $FeSi_4P_4$, *fac*-[$FeSi_3P_3$] octahedral units occupy corners of the unit cell (Figure 1a,b). The octahedral units are connected via staggered ethane-like [$P_3-Si-P-Si_3$] units, composed of SiP_4 and PSi_4 tetrahedra sharing one Si−P bond between their centra. The P and Si atoms surrounding the central atom form the vertices of the *fac*-[$FeSi_3P_3$] octahedra, forming Si−Fe and P−Fe bonds. Within the Si−P network, the layers of interconnected Si−P chains are stacked along [100]. These Si−P layers have voids where the Fe atoms reside (Figure 1c). EDS analysis confirms the composition of the Fe compound to be $FeSi_{3.93(8)}P_{4.39(6)}$ averaged over several sites on different crystallites (Figure S5). The small overestimation of light element P is common for transition metal phosphides. The stability of the structure can be explained using the Zintl−

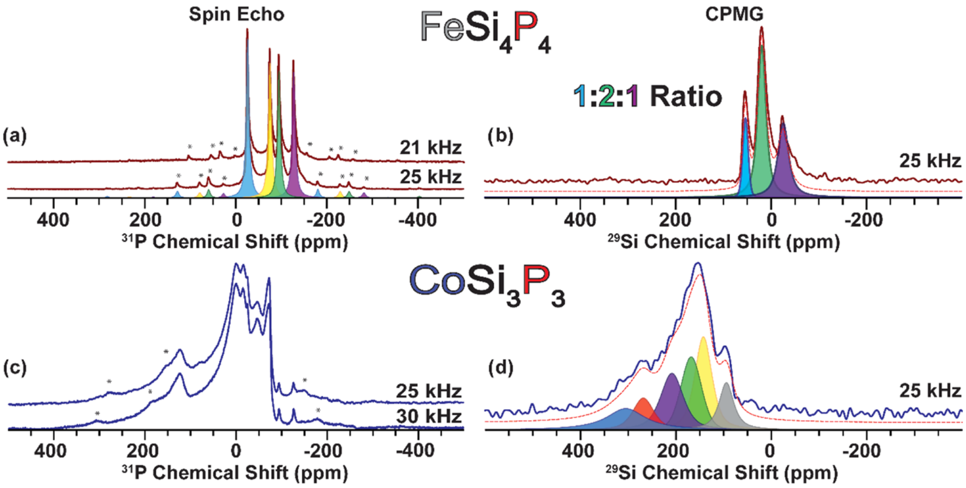

Figure 3. (a, c) Direct excitation of ^{31}P and (b, d) ^{29}Si MAS ssNMR spectra of (a, b) $FeSi_4P_4$ and (c, d) $CoSi_3P_3$. The MAS frequency used for the acquisition of the spectra is indicated. Asterisks (*) denote spinning sideband signals.

Klemm counting scheme, assuming the ionic nature of the Fe−Si and Fe−P interactions. One Si atom forms four covalent bonds to P, thus being Si^0, and three Si atoms form three covalent bonds to P, thus being Si^{1-} each. In addition, one P atom is bonded to four Si atoms, thus being P^{1+}, and three P atoms form three bonds to Si, thus being P^0 each. This leads to a 2+ oxidation state for iron, yielding an electronic balanced and semiconducting composition: $(Fe^{2+})(Si^0)(Si^{1-})_3(P^0)_3(P^{1+})$. Si is a strong field ligand; thus, a low-spin closed-shell d^6 configuration for Fe is expected.

$CoSi_3P_3$ was originally reported to crystallize in monoclinic noncentrosymmetric chiral and polar space group, $P2_1$ (No. 4), with the acknowledgment of a possibility to refine the crystal structure in the orthorhombic chiral and nonpolar space groups $P2_12_12_1$ (No. 19).[31] The subtle difference between the two models lies in the assignment of P and Si sites, which have similar X-ray scattering factors. After refinement, the authors concluded the crystal structure to be monoclinic $P2_1$ with 2 Co, 6 Si, and 6 P sites.[31] Initial refinements of our own data showed that $CoSi_3P_3$ could be solved in both space groups stated above. However, the refined β angle was clearly different from 90° being 90.125(2)°. We refined the crystal structure in $P2_1$, which resulted in an R_1 value of 0.031 and a Flack parameter value of 0.035(7) (Table S1). The crystal structure of $CoSi_3P_3$ is composed of the *fac*-$[CoSi_3P_3]$ distorted octahedra, $[SiP_4]$ tetrahedra occupying the corners of the unit cell, and $[PSi_4]$ tetrahedra occupying the center of the unit cell (Figure 2a,b). Unlike in the structure of $FeSi_4P_4$, the SiP_4 and PSi_4 tetrahedra do not overlap, and they share two corners with tetrahedra of the same kind forming one-dimensional $_\infty^1[SiP_2P_{2/2}]$ and $_\infty^1[PSi_2Si_{2/2}]$ chains running along the [010] direction (Figure 2c).

EDS confirmed the composition to be $CoSi_{2.83(3)}P_{3.14(6)}$ averaged over several sites on different crystals (Figure S6). Zintl−Klemm formalism can be applied as follows: one Si atom forming four covalent bonds to P (Si^0), another Si atom forming two bonds to P (Si^{2-}), and four Si atoms forming three Si−P bonds (Si^{1-}); one P atom forming four bonds to Si assigned as P^{1+}, another P atom forming two bonds to Si (P^{1-}), and four P atom forming three bonds to Si (P^0). Thereby, an electron-balanced formula can be written as $(Co^{3+})_2(Si^0)(Si^{2-})(Si^{1-})_4(P^{1+})(P^{1-})(P^0)_4$. Low-spin Co^{3+} is expected to have a closed-shell d^6 electronic configuration.

$FeSi_4P_4$ and $CoSi_3P_3$ contain transition metals and main group elements that have a small difference in electronegativities. The Pauling electronegativities[40] of Fe (1.8), Co (1.9), Si (1.9), and P (2.2) are comparable, which give the metal the ability to form covalent bonds with Si and P. In the crystal structure of $FeSi_4P_4$, the Fe−Si distances (2.26−2.29 Å) are shorter than the Fe−P ones (2.29−2.33 Å) (Table S2). This is unexpected based on the covalent radii trend because Si (1.17 Å) is larger than P (1.11 Å). The observed difference can be explained assuming that π-electron back-donation between Fe and Si is more effective than that between Fe and P. A similar M−Si distance shortening was observed in other metal silicon phosphides.[16,24] For $CoSi_3P_3$, larger ranges for distances were observed, Co−Si (2.20−2.35 Å) and Co−P (2.23−2.32 Å) (Table S2), yet the average Co−Si and Co−P distances are close (2.27 Å) in contradiction with the covalent radii trend.

Following the original discussion, the crystal structure of $CoSi_3P_3$ was also refined in the orthorhombic $P2_12_12_1$ space group mentioned by Perrier et al.[31] In this case, the structure displayed *mer*-$[CoSi_3P_3]$ octahedral units and $[Si@SiP_3]$ and $[P@PSi_3]$ tetrahedral units (Figure S7), neither of which were observed in other transition metal silicon phosphides. All reported transition metal silicon phosphides show no homoatomic Si−Si or P−P bonding, while such homoatomic bonds are common in alkaline-earth and rare-earth silicon phosphides.[15,20,24,41−45] Solid-state NMR (ssNMR) was further applied to corroborate the two structural models derived from X-ray diffraction. SCXRD is a dominant technique for the characterization of long-range ordering in solids. In SCXRD, there is a prominent reliance on chemical knowledge to identify elements with similar scattering factors, such as Si and P, which may lead to incorrect structural models.[16,46]

^{31}P and ^{29}Si ssNMR spectroscopy were used to characterize both $FeSi_4P_4$ and $CoSi_3P_3$ (Figure 3a,b). The SCXRD model for $FeSi_4P_4$ shows four unique crystallographic sites for the Si and P atoms. Therefore, we expect to see at most four unique peaks in each of the ^{31}P and ^{29}Si ssNMR spectra. The ^{31}P ssNMR spectrum of $FeSi_4P_4$ unambiguously shows there are four peaks with an isotropic chemical shift of −26.3, − 75.0, − 95.0, and −127.8 ppm (Figure 3a). The ^{29}Si ssNMR spectrum shows three resolved peaks with chemical shifts of 53.9, 19.0, and −23.9 ppm. Fitting the ^{29}Si NMR spectrum results in a

1:2:1 integrated intensity ratio for the 3 peaks (Figure 3b and Table S3). Therefore, the ^{29}Si NMR spectrum is also composed of four peaks, with two of them overlapping due to similar chemical shifts. To improve the sensitivity of ^{29}Si NMR experiments, we used the Carr−Purcell−Meiboom−Gill (CPMG) pulse sequence. CPMG acquisition provides a significant boost in the signal-to-noise ratio as compared to a spin echo spectrum (Figure S8). While CPMG is a nonqualitative technique, we find that peak intensities in the CPMG spectrum and a spin echo spectrum closely matched (Table S4). ^{31}P and ^{29}Si chemical shift ranges for $FeSi_4P_4$ are similar to those of other semiconducting transition metal silicon phosphide phases of isostructural $RuSi_4P_4$ (space group $P1$) and $IrSi_3P_3$ (space group Cm).

The previously reported chemical shift for $RuSi_4P_4$ was −70.6, −93.1, −121.4, and −135.5 ppm (^{31}P) and 52.8, 39.2, 28.1, and −12.3 ppm (^{29}Si). The $IrSi_3P_3$ chemical shift range is also similar to $FeSi_4P_4$, −160.2 to −184.9 ppm (^{31}P) and −1.7 to −29.2 ppm (^{29}Si).[16] The analysis of $CoSi_3P_3$ required thoughtful consideration of both SCXRD models in the $P2_1$ and $P2_12_12_1$ space groups. In the monoclinic $P2_1$ model, there are 6 P and 6 Si unique crystallographic sites. In comparison, the orthorhombic $P2_12_12_1$ model has only 3 P and 3 Si unique crystallographic sites. The ^{31}P ssNMR spectrum of $CoSi_3P_3$ exhibits at least eight distinguishable peaks with chemical shifts ranging from 200 to −150 ppm (Figure 3c). We anticipate that the signals between 50 and −150 ppm in the ^{31}P NMR spectra correspond to $CoSi_3P_3$ based on the chemical shift range for previously studied transition metal silicon phosphides.[47−49] The peaks outside this range are attributed to unidentified admixtures. The ^{29}Si NMR spectrum of $CoSi_3P_3$ consists of several broad signals with chemical shifts ranging from 400 to 50 ppm (Figure 3d). The ^{29}Si NMR spectrum was fitted to six peaks with chemical shifts of 305.2, 268.5, 208.5, 168.2, 142.7, and 94.5 ppm and a consistent 1:1:1:1:1:1 ratio of the integrated intensities. Although the $CoSi_3P_3$ ^{31}P NMR and ^{29}Si NMR spectra contain significant peak broadening and show multiple overlapping peaks, they suggest that $CoSi_3P_3$ crystallizes in the $P2_1$ space group rather than in the alternative $P2_12_12_1$ space group. The latter model predicts that there should be only three unique P signals, which is inconsistent with the observed data. Further NMR investigations are currently in progress to validate this hypothesis and to assign the P NMR signals. Further information on the experimental parameters can be found in Table S5.

Perrier and co-workers utilized Raman spectroscopy to confirm the monoclinic nature of $CoSi_3P_3$ with multiple bands observed in the 100−550 cm^{-1} frequency range.[31] Raman studies of $FeSi_4P_4$ also indicated that most of the framework Fe−Si−P vibrations occur in the 100−550 cm^{-1} range.[32] We performed FTIR characterization of both materials in the accessible spectrometer range of 400−4000 cm^{-1} (Figure S18a). In the 400−550 cm^{-1} frequency range, the observed FTIR spectra qualitatively agree with the reported Raman spectra (Figure S18b) (note that for $P1$ and $P2_1$, all vibrational bands are Raman and IR active).

The proposed from the Zintl−Klemm formalism charge-balanced semiconducting nature of the studied materials was confirmed with electronic structure calculations (vide infra) and experimental optical measurements. The UV−vis measurements showed that $FeSi_4P_4$ and $CoSi_3P_3$ are indirect band gap semiconductors. From the analysis of Tauc plots, the indirect and direct band gaps were estimated (Table 1 and Figures 4a and S9). The direct band gaps of 1.3 eV ($FeSi_4P_4$) and 1.6 eV ($CoSi_3P_3$) are consistent with observed black and deep red colors of the corresponding material.

Table 1. Experimental and Calculated Band Gaps (eV)

compound	$FeSi_4P_4$		$CoSi_3P_3$	
band gap	direct	indirect	direct	indirect
experimental	1.29(5)	1.18(5)	1.63(5)	1.46(5)
calculated (LDA)	1.26	0.96	1.36	1.23
calculated (HSE)	2.10	1.80	2.05	1.90

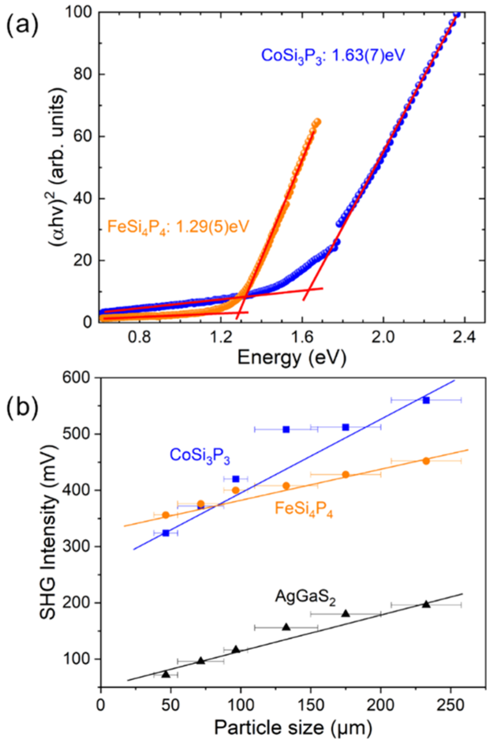

Figure 4. (a) Direct band gap Tauc plots for $FeSi_4P_4$ and $CoSi_3P_3$. (b) Second harmonic generation of $FeSi_4P_4$, $CoSi_3P_3$, and $AgGaS_2$ powders measured in identical conditions at various particle sizes.

Both materials have NCS structures and relatively narrow band gaps. The Kurtz and Perry method was utilized for second-harmonic generation (SHG) powder measurements for both $FeSi_4P_4$ and $CoSi_3P_3$ compounds using a Q-switch 2.09 μm laser source (3 Hz, 50 ns).[50] The SHG response may be weakened due to their narrow optical band gap, so reflectance SHG signals were collected. Both materials exhibit strong SHG activity, ∼3.0 times for $CoSi_3P_3$ and ∼2.5 times for $FeSi_4P_4$ higher than that of our grown by Bridgman technique $AgGaS_2$ (AGS) state-of-the-art standard in the 207−257 μm particles size range (Figure 4b and Table S6).

$FeSi_4P_4$ and $CoSi_3P_3$ performance in the 54−88 μm particles size range is better than most ternary silicon pnictides such as $IrSi_3P_3$ (1.6× AGS),[16] $IrSi_3As_3$ (1.7× AGS),[17] $RuSi_4P_4$ (1.4× AGS),[16] $MgSiAs_2$ (0.6× AGS),[14] and $Ba_2Si_3P_6$ (0.9× AGS)[15] (Figure S10 and Table S6). The only silicon phosphide with a higher SHG signal is $MnSiP_2$ (6× AGS), but $MnSiP_2$ was measured at different excitation wavelengths.[13] All previously reported silicon-phosphide materials were not phase-matchable, which prevents their practical application as NLO materials. In turn, $FeSi_4P_4$ and $CoSi_3P_3$ demonstrated a linear increase in SHG response with particle size, i.e., phase-matching, which further makes them attractive for practical applications. In addition, these materials have strong SHG responses that outperform the majority of chalcogenide NLO materials (Figure 5).

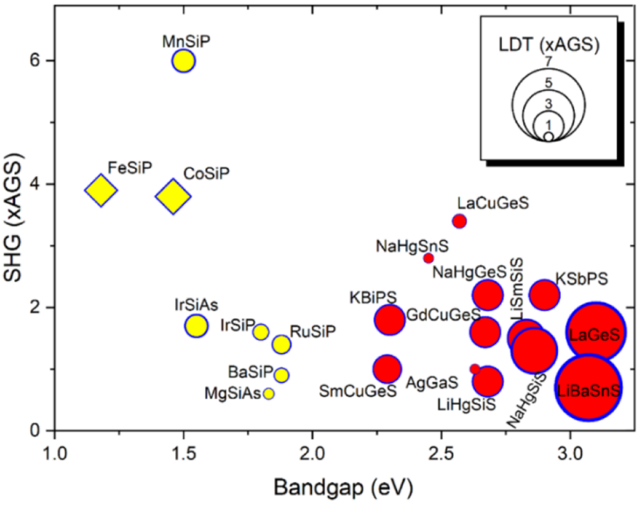

Figure 5. Diagram showing the dependence of SHG signal (vertical scale) to band gap (horizontal scale) with LDT (symbol diameter). $FeSi_4P_4$, $CoSi_3P_3$, and metal silicon phosphide materials are labeled in yellow symbols. $AgGaS_2$ and other selected chalcogenide materials are labeled with red symbols. Expansions for abbreviations can be found in Table S6.

First-principles calculations were used to investigate the optical properties of both $FeSi_4P_4$ and $CoSi_3P_3$ in the framework of density-functional theory (DFT) and density-functional perturbation theory (DFPT).[51] The exchange-correlation energy was modeled with the local-density approximation (LDA).[52] The relaxation of the crystal structure yielded cell parameters within 2% of the experimental parameters, following the usual underestimation inherent to LDA functionals. More details on the computations can be found in the Supporting Information. The calculated electronic band structures are reported in Figure 6. As proposed in the structural analysis discussion, the covalency of M−Si and M−P interactions manifests in good mixing of M-3d states with P-3p and Si-3p states in the band structures of the studied compounds. The corresponding band gaps can be found in Table 1. The excellent agreement of the direct band gaps with their experimental counterpart is quite surprising. Usually, local or semilocal functionals tend to severely underestimate the experimental value. For both compounds, the fundamental gap is indirect, which agrees with the experiment. When adopting the Heyd−Scuseria−Ernzerhof (HSE) exchange-correlation functional,[53] the calculated fundamental gap remained indirect, but the incidental agreement of the direct gaps with the experiment was lost, as shown in Table 1. The direct band gap of both materials heavily influences their optical properties. Thereby, we decided to keep the calculated LDA band gaps for the subsequent calculations.

The nonlinear optical properties were then investigated. The static high-frequency SHG tensor d_{ij}^{∞} was computed using DFPT, and for $FeSi_4P_4$, it yielded

$$d_{ij}^{\infty} = \begin{bmatrix} 24.26 & -6.13 & 9.00 & 7.11 & 18.38 & 15.85 \\ 15.85 & 54.82 & 19.49 & 17.27 & 7.11 & -6.13 \\ 18.38 & 17.27 & 27.96 & 19.49 & 9.00 & 7.11 \end{bmatrix}$$

while for $CoSi_3P_3$, it was

$$d_{ij}^{\infty} = \begin{bmatrix} 0 & 0 & 0 & -33.44 & 0 & 3.76 \\ 3.76 & -92.62 & 3.82 & 0 & -33.44 & 0 \\ 0 & 0 & 0 & 3.82 & 0 & -33.44 \end{bmatrix}$$

Equation 1 demonstrates that the ratio of the experimental SHG intensities, I, can be linked to a ratio of effective coefficients, d_{eff}, derived from the tensors and the superscript (R) indicates the reference sample.[50,54]

$$\left(\frac{d_{\text{eff}}}{d_{\text{eff}}^{(R)}}\right)^2 = \frac{I}{I^{(R)}} \tag{1}$$

It was decided that the root-mean-square of the SHG components was an effective coefficient. This value constitutes an invariant of third-rank tensors while embodying the averaging concept of the powder technique.[55] As a result, $FeSi_4P_4$ and $CoSi_3P_3$ possess effective coefficients of 18.09 and 23.86 pm/V, respectively. The only nonzero component of $AgGaS_2$, d_{36}, can vary quite drastically in the literature. For this reason, the DFPT SHG tensor of $AgGaS_2$ was also computed in this work following the same procedure as for $FeSi_4P_4$ and $CoSi_3P_3$, except that a scissor of 1.7 eV was applied to match the experimental band gap of 2.64 eV.[56] Using the ratio of effective coefficients, we can calculate the different SHG values between our reference, $AgGaS_2$, and the studied ternary tetrel pnictides (Table S7). In practice, a ratio of intensities of ∼4 is equivalent to an effective coefficient in-between 6.6 and 32.8 pm/V for $FeSi_4P_4$ and $CoSi_3P_3$, which is in line with the DFPT results.

The frequency-dependent d_{22}, the largest component of the SHG tensor, was also computed (see Figures S11 and S12). A band-resolved analysis was further performed to understand the origin of the SHG response for the two compounds at hand.[57] The total frequency-dependent SHG response is the sum of two- or three-band contributions. In a band-resolved analysis, the latter are isolated and then partially summed over, such that the total contribution of each individual valence and conduction band is recovered. This allows one to quantify the contribution of each band to the SHG response at a given frequency, as illustrated in Figure 6. The investigated frequency was chosen based on the following sum rule:

$$\Re(\chi^{(2)}(0, 0, 0)) = \frac{2}{\pi} P \int \frac{\Im(\chi^{(2)}(-2\omega, \omega, \omega))}{\omega} d\omega$$

which dictates that the magnitude of the static real part of a coefficient is directly related to the main peak of its imaginary spectrum.[58] It is thus interesting to perform a band-resolved analysis of this peak to understand $\chi^{(2)}$ (0,0,0). As can be seen in Figures S13 and S14, this peak is located at 1.06 and 0.87 eV for $FeSi_4P_4$ and $CoSi_3P_3$, respectively. The "Intra 2ω" and "Inter 2ω" denominations refer to the 2ω-resonant intra- and interband transitions, respectively. Together with the "IntraS" term, i.e., the modulation of the interband terms by intraband ones, and their 1ω-resonant counterpart, they constitute the total SHG response as introduced by Sipe and Ghahramani.[59] The origin of these three terms lies in the mathematical

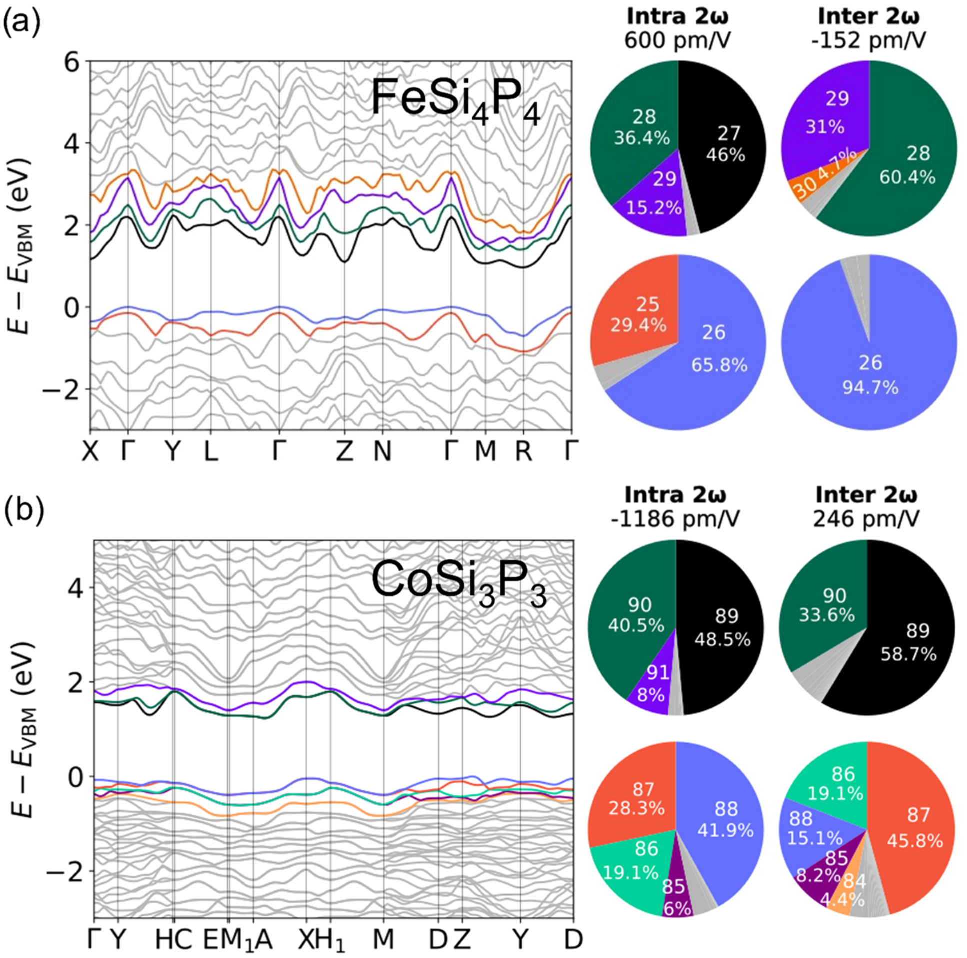

Figure 6. (a) Band-resolved analysis of the imaginary part of the d_{22} coefficient of $FeSi_4P_4$ at 1.06 eV. (b) Band-resolved analysis of the imaginary part of the d_{22} coefficient of $CoSi_3P_3$ at 0.87 eV. The electronic structure bands are color-coded (left) to relate with the pie charts (right), which are associated with the individual contributions of the most important bands to the SHG response. Only the three-band interactions were considered as the two-band ones are negligible. The bands are shifted to set the valence band maximum (VBM) at 0 eV.

development of the Hamiltonian when deriving the sum-overstates equation.

To the best of our knowledge, a clear physical interpretation of those terms is still lacking. Fortunately, it is not required in the context of the present band-resolved analysis. In line with expectations, the first bands on both sides of the gap are the major contributors to the SHG response, which is expected (Figure 6). To complement this analysis, a projected density of states (PDOS) was computed (Figures S15 and S16). In $FeSi_4P_4$, the SHG response mainly comes from the Fe-3d, Si-3p, and P-3p contributions. Similarly, in $CoSi_3P_3$, the orbitals Co-3d, Si-3p, and P-3p are mainly responsible for the SHG. Our computational exploration supports the experimentally observed linear and nonlinear optical properties of $FeSi_4P_4$ and $CoSi_3P_3$ as well as the hypothesis regarding strong covalent bonding interactions between transition metal, silicon, and phosphorus.

Besides phase-matchability and SHG intensity, the laser damage threshold (LDT) is an important characteristic of the NLO material. LDT measurements are less standardized than SHG ones, and different values of LDT were reported for the powders of AGS standard, ranging from 1 to 30 MW cm^{-2} even for the same laser wavelength of 1.06 μm. The different pulse sequences and varying quality of the AGS standard may be responsible for the large discrepancy in the LDT reports for AGS. Nevertheless, single crystals of AGS were reported to have LDT of ∼30 MW cm^{-2}. To avoid comparing apples to oranges, we limited the following discussion to such examples of reported LDTs where measurements of AGS LDT at the same setup and identical conditions generated an LDT of 28−32 MW cm^{-2}. Generally, chalcogenide materials have an established trend of a positive relationship between band gap and LDT, i.e., small band gap materials show high SHG activity but low LDT and *vice versa*. For example, Li_2BaSnS_4 has a 3.07 eV band gap, which exhibits a low SHG intensity (0.7× AGS) but a high LDT value (192 MW cm^{-2})[60] (Figures 5, 7, and S10). The LDT values for $FeSi_4P_4$ (68 MW cm^{-2}, 2.3× AGS) and $CoSi_3P_3$ (74 MW cm^{-2}, 2.5× AGS) are particularly exceptional for small band gap semiconductors (Table S6). Due to strong covalent M−P and M−Si bonds, transition metal silicon phosphides exhibit higher LDT values, such as $MnSiP_2$ (70 MW cm^{-2}),[13] $IrSi_3P_3$ (48 MW cm^{-2}),[16] $IrSi_3As_3$ (68 MW cm^{-2}),[17] and $RuSi_4P_4$ (58 MW cm^{-2}),[16] than alkaline-earth silicon phosphides, $MgSiAs_2$ (33 MW cm^{-2}),[14] and $Ba_2Si_3P_6$ (45 MW cm^{-2})[18] (Figures 7 and S10 and Table S6). Transition metal silicon-phosphides break the trend observed in chalcogenide materials by showing consistent LDT even for materials with small band gaps, <2 eV. As confirmed by our calculational evaluations, the strong covalency of {Co,Fe}-{Si,P} bonds contributes to the high LDT of the

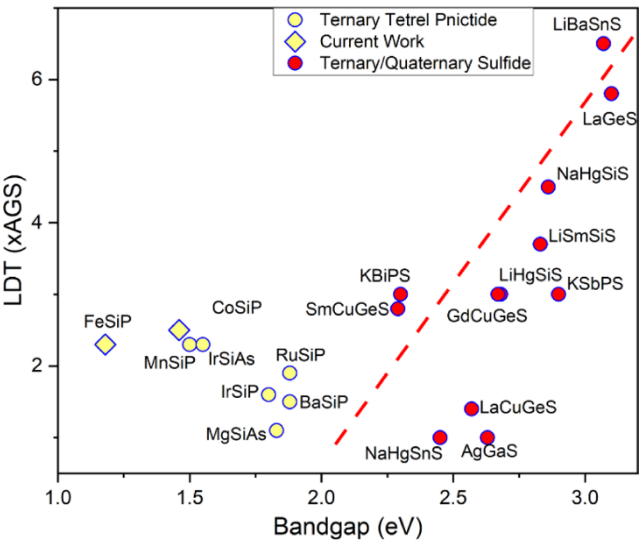

Figure 7. Band gap dependence of the normalized LDT values for ternary phosphides (labeled in yellow) and selected ternary and quaternary sulfides (labeled in red) that were experimentally verified to be phase-matching materials. Expansions for abbreviations can be found in Table S6.

studied compounds. We hypothesized that the higher ionic component of M—S and M—Se bonding makes chalcogenides more susceptible to laser irradiation, and a higher band gap is required for chalcogenides to achieve high LDT.

■ CONCLUSIONS

We developed a synthetic approach to produce powdered samples and millimeter-sized crystals of $FeSi_4P_4$ and $CoSi_3P_3$. The crystal structures of these NCS moderate band gap semiconductors were redetermined through SCXRD and ^{29}Si, ^{31}P MAS NMR techniques. $FeSi_4P_4$ is confirmed to crystallize in the $P1$ space group, while $CoSi_3P_3$ is confirmed to crystallize in the $P2_1$ space group with no homoatomic Si—Si or P—P bonds in either structure. $FeSi_4P_4$ and $CoSi_3P_3$ demonstrate strong SHG activity and exceptional LDT as compared to the $AgGaS_2$ state-of-the-art standard. First-principles computations confirm the high SHG for these phases and provide their full d_{ijk} tensor. The calculations attribute the strong NLO response of the title compounds to the covalency of {Fe,Co}—{P—Si} interactions. When compared to chalcogenide NLO materials, $FeSi_4P_4$ and $CoSi_3P_3$ are acid stable, have high oxidation resistance, are composed of inexpensive and earth-abundant elements, and exhibit a healthy balance of SHG response and LDT values with phase-matching.

■ ASSOCIATED CONTENT

SI Supporting Information

The Supporting Information is available free of charge at https://pubs.acs.org/doi/10.1021/acs.chemmater.4c01688.

> Experimental and computational methods and additional figures and tables pertaining to powder X-ray diffraction, scanning electron microscopy/energy-dispersive X-ray spectroscopy, ssNMR, TGA/DSC, FTIR, diffuse reflectance spectroscopy, and electronic structure calculations. (PDF)

■ AUTHOR INFORMATION

Corresponding Author

Kirill Kovnir − *Department of Chemistry, Iowa State University, Ames, Iowa 50011, United States; Ames National Laboratory, U.S. Department of Energy, Ames, Iowa 50011, United States;* orcid.org/0000-0003-1152-1912; Email: kovnir@iastate.edu

Authors

Ernesto Soto − *Department of Chemistry, Iowa State University, Ames, Iowa 50011, United States; Ames National Laboratory, U.S. Department of Energy, Ames, Iowa 50011, United States;* orcid.org/0000-0001-5346-7382

Shannon J. Lee − *Department of Chemistry, Iowa State University, Ames, Iowa 50011, United States; Ames National Laboratory, U.S. Department of Energy, Ames, Iowa 50011, United States; Physical Science Division, Pacific Northwest National Laboratory, U.S. Department of Energy, Richland, Washington 99352, United States;* orcid.org/0000-0002-7541-3286

Andrew P. Porter − *Department of Chemistry, Iowa State University, Ames, Iowa 50011, United States; Ames National Laboratory, U.S. Department of Energy, Ames, Iowa 50011, United States*

Gayatri Viswanathan − *Department of Chemistry, Iowa State University, Ames, Iowa 50011, United States; Ames National Laboratory, U.S. Department of Energy, Ames, Iowa 50011, United States*

Georgiy Akopov − *Department of Chemistry, Rutgers University, Newark, New Jersey 07102, United States;* orcid.org/0000-0001-9399-9850

Nethmi Hewage − *Department of Chemistry, Iowa State University, Ames, Iowa 50011, United States; Ames National Laboratory, U.S. Department of Energy, Ames, Iowa 50011, United States*

Kui Wu − *State Key Laboratory of Crystal Materials and Institute of Crystal Materials, Shandong University, Jinan 071002, China;* orcid.org/0000-0001-8242-4613

Victor Trinquet − *Institute of Condensed Matter and Nanosciences (IMCN), UCLouvain, Louvain-la-Neuve B-1348, Belgium*

Guillaume Brunin − *Institute of Condensed Matter and Nanosciences (IMCN), UCLouvain, Louvain-la-Neuve B-1348, Belgium*

Geoffroy Hautier − *Thayer School of Engineering, Dartmouth College, Hanover, New Hampshire 03755, United States;* orcid.org/0000-0003-1754-2220

Gian-Marco Rignanese − *Institute of Condensed Matter and Nanosciences (IMCN), UCLouvain, Louvain-la-Neuve B-1348, Belgium;* orcid.org/0000-0002-1422-1205

Aaron J. Rossini − *Department of Chemistry, Iowa State University, Ames, Iowa 50011, United States; Ames National Laboratory, U.S. Department of Energy, Ames, Iowa 50011, United States;* orcid.org/0000-0002-1679-9203

Complete contact information is available at: https://pubs.acs.org/10.1021/acs.chemmater.4c01688

Author Contributions

K.K. conceived of and supervised the project. E.S., S.J.L., N.H., and G.A. conducted the synthesis and majority of experiments. E.S. organized all the data and wrote the manuscript with K.K. G.V. conducted diffuse reflectance experiments. K.W. conducted nonlinear optical studies. A.P.P. and A.J.R. conducted ssNMR studies. V.T., G.B., G.H., and G.-M.R. conducted the calculations.

Funding

This research was supported by the National Science Foundation under Grant No. 1955456 to K.K. Solid-state NMR spectroscopy experiments (A.P.P. and A.J.R.) were supported by the U.S. Department of Energy (DOE), Office of Science, Basic Energy Sciences, Materials Science and Engineering Division. Ames National Laboratory is operated for the U.S. DOE by Iowa State University under Contract DE-AC02-07CH11358. A.J.R. acknowledges additional support from the Alfred P. Sloan Foundation through a Sloan research fellowship. G.A. is grateful for the support from the Rutgers University, Newark new faculty start-up fund. The theoretical part of the work has been supported in part by the U.S. Department of Energy, Office of Science, Basic Energy Sciences under Award Number DE-SC0023509. Computational resources have been provided by the supercomputing facilities of the Université catholique de Louvain (CISM/UCL) and the Consortium des Équipements de Calcul Intensif en Fédération Wallonie Bruxelles (CÉCI) funded by the Fond de la Recherche Scientifique de Belgique (F.R.S.-FNRS) under convention 2.5020.11 and by the Walloon Region. The present research benefited from computational resources made available on Lucia, the Tier-1 supercomputer of the Walloon Region, infrastructure funded by the Walloon Region under grant agreement No. 1910247. V.T. acknowledges the support from the FRS-FNRS through an FRIA Grant.

Notes

The authors declare no competing financial interest.

ACKNOWLEDGMENTS

We thank Dr. Yaroslav Mudryk (Ames National Laboratory) for access to the arc-melting setup and Professor Julia Zaikina (ISU) for the use of the diffuse-reflectance setup.

REFERENCES

(1) Chu, D.; Huang, Y.; Xie, C.; Tikhonov, E.; Kruglov, I.; Li, G.; Pan, S.; Yang, Z. Unbiased Screening of Novel Infrared Nonlinear Optical Materials with High Thermal Conductivity: Long-neglected Nitrides and Popular Chalcogenides. *Angew. Chem., Int. Ed.* **2023**, *62* (1), No. e202300581.

(2) Luo, L.; Wang, L.; Chen, J.; Zhou, J.; Yang, Z.; Pan, S.; Li, J. $A^{I}B_3^{II}C_3^{III}Q_8^{VI}$: A New Family for the Design of Infrared Nonlinear Optical Materials by Coupling Octahedra and Tetrahedra Units. *J. Am. Chem. Soc.* **2022**, *144* (48), 21916−21925.

(3) Zhang, H.; Zhang, M.; Pan, S.; Dong, X.; Yang, Z.; Hou, X.; Wang, Z.; Chang, K. B.; Poeppelmeier, K. R. $Pb_{17}O_8Cl_{18}$: A Promising IR Nonlinear Optical Material with Large Laser Damage Threshold Synthesized in an Open System. *J. Am. Chem. Soc.* **2015**, *137* (26), 8360−8363.

(4) Aslam, H. Z.; Doane, J. T.; Yeung, M. T.; Akopov, G. Advances in Solid-State Nonlinear Optical Materials: From Fundamentals to Applications. *ACS Appl. Opt. Mater.* **2023**, *1* (12), 1898−1921.

(5) He, J.; Iyer, A. K.; Waters, M. J.; Sarkar, S.; Zu, R.; Rondinelli, J. M.; Kanatzidis, M. G.; Gopalan, V. MgSiP2: An Infrared Nonlinear Optical Crystal with a Large Non-Resonant Phase-Matchable Second Harmonic Coefficient and High Laser Damage Threshold. *Adv. Opt. Mater.* **2022**, *10* (2), No. 2101729.

(6) Khatun, M.; Stoyko, S. S.; Mar, A. Ternary Arsenides ATt_3As_3 (A = K, Rb; Tt = Ge, Sn) with Layered Structures. *J. Solid State Chem.* **2016**, *238*, 229−235.

(7) Weippert, V.; Chau, T.; Witthaut, K.; Johrendt, D. Mixed Valence and Unusual Germanium Coordination in $SrGe_8As_{10}$, $BaGe_8As_{10}$, and $BaGe_7P_{12}$. *Inorg. Chem.* **2020**, *59* (20), 15447−15453.

(8) Park, Y.; Kanatzidis, M. G. On the Dissolution of Gold in K_2Q_x and Na_2Q_x Fluxes (Q = S, Se). Formation of $KAuS_5$, $KAuSe_5$, $CsAuSe_3$, $KAuSe_2$ and $NaAuSe_2$: Low-Dimensional Au^+ and Au^{3+} Compounds with Poly- and Mono-Chalcogenide Ligands. *J. Alloys Compd.* **1997**, *257*, 137−145.

(9) Park, Y.; Kanatzidis, M. G. $AuCuSe_4$: A Mixed Polychalcogenide with Se_3^{2}- and Se^{2-} Anions. *Inorg. Chem.* **2001**, *40* (23), 5913−5916.

(10) Kurzman, J. A.; Ouyang, X.; Im, W. B.; Li, J.; Hu, J.; Scott, S. L.; Seshadri, R. La_4LiAuO_8 and La_2BaPdO_5: Comparing Two Highly Stable d^8 Square-Planar Oxides. *Inorg. Chem.* **2010**, *49* (10), 4670−4680.

(11) Hahn, H.; Frank, G.; Klingler, W.; Meyer, A.-D.; Störger, G. Untersuchungen über ternäre Chalkogenide. V. Über einige ternäre Chalkogenide mit Chalkopyritstruktur. *Z. Anorg. Allg. Chem.* **1953**, *271* (3−4), 153−170.

(12) Harasaki, A. H. A.; Kato, K. K. K. New Data on the Nonlinear Optical Constant, Phase-Matching, and Optical Damage of $AgGaS_2$. *Jpn. J. Appl. Phys.* **1997**, *36* (2R), 700.

(13) Yu, T.; Wang, S.; Zhang, X.; Li, C.; Qiao, J.; Jia, N.; Han, B.; Xia, S.-Q.; Tao, X. $MnSiP_2$: A New Mid-IR Ternary Phosphide with Strong SHG Effect and Ultrabroad Transparency Range. *Chem. Mater.* **2019**, *31* (6), 2010−2018.

(14) Woo, K. E.; Wang, J.; Wu, K.; Lee, K.; Dolyniuk, J.-A.; Pan, S.; Kovnir, K. Mg-Si-As: An Unexplored System with Promising Nonlinear Optical Properties. *Adv. Funct. Mater.* **2018**, *28* (30), No. 1801589.

(15) Mark, J.; Wang, J.; Wu, K.; Lo, J. G.; Lee, S.; Kovnir, K. Ba_2Si_3P6:1D Nonlinear Optical Material with Thermal Barrier Chains. *J. Am. Chem. Soc.* **2019**, *141* (30), 11976−11983.

(16) Lee, S.; Carnahan, S. L.; Akopov, G.; Yox, P.; Wang, L.-L.; Rossini, A. J.; Wu, K.; Kovnir, K. Noncentrosymmetric Tetrel Pnictides $RuSi_4P_4$ and $IrSi_3P_3$: Nonlinear Optical Materials with Outstanding Laser Damage Threshold. *Adv. Funct. Mater.* **2021**, *31* (16), No. 2010293.

(17) Lee, S. J.; Akopov, G.; Adeyemi, A. N.; Soto, E.; Wu, K.; Kovnir, K. $IrSi_3As_3$: A First Transition Metal Arsenide Non-Linear Optical Material. *J. Mater. Chem. A* **2023**, *11*, 11767.

(18) Chen, J.; Lin, C.; Peng, G.; Xu, F.; Luo, M.; Yang, S.; Shi, S.; Sun, Y.; Yan, T.; Li, B.; Ye, N. $BaGe_2Pn_2$ (Pn= P, As): Two Congruent-Melting Non-chalcopyrite Pnictides as Mid- and Far-Infrared Nonlinear Optical Materials Exhibiting Large Second Harmonic Generation Effects. *Chem. Mater.* **2019**, *31* (24), 10170−10177.

(19) Sun, Y.; Chen, J.; Yang, S.; Li, B.; Chai, G.; Lin, C.; Luo, M.; Ye, N. $LaSiP_3$ and $LaSi_2P_6$: Two Excellent Rare-Earth Pnictides with Strong SHG Responses as Mid- and Far-Infrared Nonlinear Optical Crystals. *Adv. Opt. Mater.* **2021**, *9* (10), No. 2002176.

(20) Akopov, G.; Mark, J.; Viswanathan, G.; J Lee, S.; C McBride, B.; Won, J.; A Perras, F.; L Paterson, A.; Yuan, B.; Sen, S.; N Adeyemi, A.; Zhang, F.; Wang, C.-Z.; Ho, K.-M.; J Miller, G.; Kovnir, K. Third Time's the Charm: Intricate Non-Centrosymmetric Polymorphism in $LnSiP_3$ (Ln = La and Ce) Induced by Distortions of Phosphorus Square Layers. *Dalton Trans.* **2021**, *50* (19), 6463−6476.

(21) Chen, J.; Chen, H.; Xu, F.; Cao, L.; Jiang, X.; Yang, S.; Sun, Y.; Zhao, X.; Lin, C.; Ye, N. $Mg_2In_3Si_2P_7$: A Quaternary Diamond-like Phosphide Infrared Nonlinear Optical Material Derived from $ZnGeP_2$. *J. Am. Chem. Soc.* **2021**, *143* (27), 10309−10316.

(22) Narang, P.; Garcia, C. A. C.; Felser, C. The Topology of Electronic Band Structures. *Nat. Mater.* **2021**, *20* (3), 293−300.

(23) Lee, S. J.; Won, J.; Wang, L.-L.; Jing, D.; Harmer, C. P.; Mark, J.; Akopov, G.; Kovnir, K. New Noncentrosymmetric Tetrel Pnictides Composed of Square-Planar Gold(I) with Peculiar Bonding. *Chem. − Eur. J.* **2021**, *27* (26), 7383−7390.

(24) Lee, S. J.; Viswanathan, G.; Carnahan, S. L.; Harmer, C. P.; Akopov, G.; Rossini, A. J.; Miller, G. J.; Kovnir, K. Add a Pinch of Tetrel: The Transformation of a Centrosymmetric Metal into a Nonsymmorphic and Chiral Semiconductor. *Chem. − Eur. J.* **2022**, *28* (9), No. e202104319.

(25) Yang, H.-D.; Ran, M.-Y.; Wei, W.-B.; Wu, X.-T.; Lin, H.; Zhu, Q.-L. The Rise of Infrared Nonlinear Optical Pnictides: Advances and Outlooks. *Chem. – Asian J.* **2021**, *16* (21), 3299–3310.

(26) Chen, J.; Wu, Q.; Tian, H.; Jiang, X.; Xu, F.; Zhao, X.; Lin, Z.; Luo, M.; Ye, N. Uncovering a Vital Band Gap Mechanism of Pnictides. *Adv. Sci.* **2022**, *9* (14), No. 2105787.

(27) Kaiser, P.; Jeitschko, W. Preparation and Crystal Structures of the Ternary Compounds Ag_2SiP_2 and AuSiP. *Z. Naturforschung B* **1997**, *52* (4), 462–468.

(28) Inorganic Crystal Structure Database. https://icsd.products.fiz-karlsruhe.de/ (accessed May 21, 2024).

(29) Prices of Chemical Elements. https://en.wikipedia.org/wiki/Prices_of_chemical_elements (accessed January 10, 2024).

(30) Perrier, C.; Vincent, H.; Chaudouët, P.; Chenevier, B.; Madar, R. Preparation and Crystal Structure of a New Family of Transition Metal Phospho-Silicides. *Mater. Res. Bull.* **1995**, *30* (3), 357–364.

(31) Perrier, C.; Kreisel, J.; Vincent, H.; Chaix-Pluchery, O.; Madar, R. Synthesis, Crystal Structure, Physical Properties and Raman Spectroscopy of Transition Metal Phospho-Silicides MSi_xP_y (M = Fe, Co, Ru, Rh, Pd, Os, Ir, Pt). *J. Alloys Compd.* **1997**, *262–263*, 71–77.

(32) Yu, T.; Wang, S.; Ruan, H.; Li, C.; Zhang, X.; Jia, N.; Zhang, J.; Tao, X. Flux Growth and Characterization of an $FeSi_4P_4$ Single Crystal. *RSC Adv.* **2017**, *7* (76), 47938–47944.

(33) Akopov, G.; Viswanathan, G.; Hewage, N. W.; Yox, P.; Wu, K.; Kovnir, K. Pd and Octahedra Do Not Get along: Square Planar $[PdS_4]$ Units in Non-Centrosymmetric $La_6PdSi_2S_{14}$. *J. Alloys Compd.* **2022**, *902*, No. 163756.

(34) Akopov, G.; Hewage, N. W.; Yox, P.; Viswanathan, G.; Lee, S. J.; Hulsebosch, L. P.; Cady, S. D.; Paterson, A. L.; Perras, F. A.; Xu, W.; Wu, K.; Mudryk, Y.; Kovnir, K. Synthesis-Enabled Exploration of Chiral and Polar Multivalent Quaternary Sulfides. *Chem. Sci.* **2021**, *12* (44), 14718–14730.

(35) Kim, S.-B.; Cho, Y.-H.; Lee, J.-M.; Jung, J.-G.; Lim, S. G. The Effect of Ultrasonic Melt Treatment on the Microstructure and Mechanical Properties of Al-7Si-0.35Mg Casting Alloys. *Korean J. Met. Mater.* **2017**, *55* (4), 240–246.

(36) Patel, D. N.; Sutaria, M. P. Effect of Trace Rare Earth Er Addition on Microstructure and Tensile Properties of 319 Al-Si-Cu Alloy. *Int. J. Met.* **2022**, *16* (4), 2199–2209.

(37) Kang, J.; Su, R.; Wu, D. Y.; Liu, C. H.; Li, T.; Wang, L. S.; Narayanaswamy, B. Synergistic Effects of Ce and Mg on the Microstructure and Tensile Properties of Al-7Si-0.3Mg-0.2Fe Alloy. *J. Alloys Compd.* **2019**, *796*, 267–278.

(38) Ono, S.; Hayakawa, H.; Nomura, K. Synthesis of Ln-Si-P (Ln = La, Ce, Pr) Ternary Compounds. *J. Chem. Soc. Jpn.* **1976**, *11*, 1700–1709.

(39) Hayakawa, H.; Ono, S.; Kobayashi, A. The Crystal Structure of Cerium Silicon Triphosphide ($CeSiP_3$). *J. Chem. Soc. Jpn.* **1978**, *9*, 1214–1220.

(40) Pauling, L. *The Nature of the Chemical Bond and the Structure of Molecules and Crystals: An Introduction to Modern Structural Chemistry*; Cornell University Press: Ithaca, NY, 1960.

(41) Mark, J.; Dolyniuk, J.-A.; Tran, N.; Kovnir, K. Crystal and Electronic Structure and Optical Properties of AE_2SiP_4 (AE = Sr, Eu, Ba) and $Ba_4Si_3P_8$. *Z. Anorg. Allg. Chem.* **2019**, *645*, 242–247.

(42) Haffner, A.; Weippert, V.; Johrendt, D. Polymorphism of Ba_2SiP_4. *Z. Anorg. Allg. Chem.* **2020**, *646*, 120–124.

(43) Haffner, A.; Johrendt, D. Synthesis, Crystal Structure, and Chemical Bonding of Ba_2SiP_4. *Z. Anorg. Allg. Chem.* **2017**, *643* (21), 1717–1720.

(44) Akopov, G.; Viswanathan, G.; Kovnir, K. Synthesis, Crystal and Electronic Structure of La_2SiP_4. *Z. Anorg. Allg. Chem.* **2021**, *647*, 91–97.

(45) Kaiser, P.; Jeitschko, W. The Rare Earth Silicon Phosphides $LnSi_2P_6$ (Ln= La, Ce, Pr, and Nd). *J. Solid State Chem.* **1996**, *124* (2), 346–352.

(46) Raymond, K. N.; Girolami, G. S. Pathological Crystal Structures. *Acta Crystallogr., Sect. C* **2023**, *79* (11), 445–455.

(47) Bekaert, E.; Bernardi, J.; Boyanov, S.; Monconduit, L.; Doublet, M.-L.; Ménétrier, M. Direct Correlation between the ^{31}P MAS NMR Response and the Electronic Structure of Some Transition Metal Phosphides. *J. Phys. Chem. C* **2008**, *112* (51), 20481–20490.

(48) Furo, I.; Bakonyi, I.; Tompa, K.; Zsoldos, E.; Heinmaa, I.; Alla, M.; Lippmaa, E. ^{31}P Nuclear Magnetic Resonance Knight Shift and Linewidth in Ni_3P and Cu_3P: A Magic-Angle Spinning Study. *J. Phys.: Condens. Matter* **1990**, *2* (18), 4217.

(49) Stinner, C.; Tang, Z.; Haouas, M.; Weber, Th.; Prins, R. Preparation and ^{31}P NMR Characterization of Nickel Phosphides on Silica. *J. Catal.* **2002**, *208* (2), 456–466.

(50) Kurtz, S. K.; Perry, T. T. A Powder Technique for the Evaluation of Nonlinear Optical Materials. *J. Appl. Phys.* **1968**, *39* (8), 3798–3813.

(51) Gonze, X.; Lee, C. Dynamical Matrices, Born Effective Charges, Dielectric Permittivity Tensors, and Interatomic Force Constants from Density-Functional Perturbation Theory. *Phys. Rev. B* **1997**, *55* (16), 10355–10368.

(52) Perdew, J. P.; Wang, Y. Accurate and Simple Analytic Representation of the Electron-Gas Correlation Energy. *Phys. Rev. B* **1992**, *45* (23), 13244–13249.

(53) Krukau, A. V.; Vydrov, O. A.; Izmaylov, A. F.; Scuseria, G. E. Influence of the Exchange Screening Parameter on the Performance of Screened Hybrid Functionals. *J. Chem. Phys.* **2006**, *125* (22), No. 224106.

(54) Clark, D. J.; Zhang, J.-H.; Craig, A. J.; Weiland, A.; Brant, J. A.; Cho, J. B.; Kim, Y. S.; Jang, J. I.; Aitken, J. A. The Kurtz-Perry Powder Technique Revisited: A Case Study on the Importance of Reference Quality and Broadband Nonlinear Optical Measurements Using $LiInSe_2$. *J. Alloys Compd.* **2022**, *917*, No. 165381.

(55) Qi, L.; Chen, H.; Chen, Y.; Qi, L.; Chen, H.; Chen, Y. Third Order Tensors in Physics and Mechanics. In *Tensor Eigenvalues and Their Applications*, Advances in Mechanics and Mathematics; Springer: Singapore, 2018; pp 207–248.

(56) Jackson, A. G.; Ohmer, M.; Leclair, S. Relationship of the Second Order Nonlinear Optical Coefficient to Bandgap in Inorganic Non-Centrosymmetric Crystals 1995 https://corescholar.libraries.wright.edu/mme/193.

(57) Lee, M.-H.; Yang, C.-H.; Jan, J.-H. Band-Resolved Analysis of Nonlinear Optical Properties of Crystalline and Molecular Materials. *Phys. Rev. B* **2004**, *70* (23), No. 235110.

(58) Lambrecht, W. R. L.; Rashkeev, S. N. From Band Structures to Linear and Nonlinear Optical Spectra in Semiconductors. *Phys. Status Solidi B* **2000**, *217* (1), 599–640.

(59) Sipe, J. E.; Ghahramani, E. Nonlinear Optical Response of Semiconductors in the Independent-Particle Approximation. *Phys. Rev. B* **1993**, *48* (16), 11705–11722.

(60) Wu, K.; Zhang, B.; Yang, Z.; Pan, S. New Compressed Chalcopyrite-like $Li_2BaM^{IV}Q_4$ (M^{IV} = Ge, Sn; Q = S, Se): Promising Infrared Nonlinear Optical Materials. *J. Am. Chem. Soc.* **2017**, *139* (42), 14885–14888.